Fabrication and deformation of three-dimensional hollow ceramic nanostructures

Dongchan Jang,[1] Lucas Meza,[1] Frank Greer,[2] and Julia R. Greer[1,3]

[1]*Division of Engineering and Applied Science*
California Institute of Technology
Pasadena, CA 91125

[2]*Jet Propulsion Laboratory*
Pasadena, CA 91109

[3]*The Kavli Nanoscience Institute*
California Institute of Technology
Pasadena, CA 91125

Introductory Paragraph

Creating lightweight, mechanically robust materials has long been an engineering pursuit. Many siliceous skeleton species – such as diatoms, sea sponges and radiolarians – have remarkably higher strength than man-made materials of the same composition yet remain lightweight and porous[1–7], and it has been hypothesized that these properties arise from the hierarchical arrangement of different structural elements at their relevant length scales[8,9]. Here, we report the fabrication of hollow ceramic scaffolds that mimic the length scales and hierarchy of biological materials and that attain tensile strengths of 1.75 GPa without failure even after multiple deformation cycles, as revealed by in situ nanomechanical experiments and finite-element analysis. We discuss the high strength and lack of failure in terms of stress concentrators at surface imperfections and local stresses within the microstructural landscape. Our findings suggest that the hierarchical design principles offered by hard biological organisms can be applied to create damage-tolerant lightweight engineering materials.

Hard biological materials such as bones, shells, nacres, and wood, often contain hierarchically arranged constituents[1–7], whose dimensions can span from nanometers to micrometers to centimeters and larger. Figure 1**a** – **c** (reprinted from Ref [1] and [10]) displays Scanning Electron Microscope (SEM) (**a**, **b**), and optical (**c**) images of silicified cell walls from diatoms and radiolaria, which display periodic skeletal arrangements characteristic of bioceramics. These siliceous skeleton organisms are mechanically robust and lightweight, properties that have been shown to contribute to their effective defense against predators[4]. More complex biominerals such as nacre, mollusk shells and crustaceans, have been reported to have higher fracture toughness than manmade monolithic ceramics of the same composition[11], which has been attributed to features at the lowest level of hierarchy, on the order of nanometers[9]. Nature's motivation for utilizing these carefully chosen discrete length scales may stem from the advantageous properties offered by the interplay of individual biological constituents[8,9].

Mechanical properties of cellular materials, i.e. foams, bone, and lattices are usually defined by the unit cell geometry, the relative density ($\bar{\rho} = \rho/\rho_s$), and the solid material properties[12]. Both the Young's modulus and strength of cellular solids scale with the relative density as: $E \propto E_s\bar{\rho}^l$ and $\sigma \propto \sigma_s\bar{\rho}^n$, where E_s and σ_s are Young's modulus and strength of parent materials and the exponents l and n are defined by the cell geometry[12]. Classical cellular solids mechanics theories generally assume that the properties of the parent solid (E_s and σ_s) are independent of its dimensions. This implies that same-solid cellular materials with similar geometries will have identical moduli and strengths regardless of their absolute dimensions. This classical description may not be able to capture the mechanical properties of porous biological structures, which have been characterized by property amplification beyond the rule of mixtures. This could, in part, be caused by the emergence of size effects in the mechanical strength of nano-sized solids, such as power-law strengthening in single-crystalline metals and a suppression of catastrophic failure in metallic glasses and ceramics once their dimensions are in the sub-micron range (see Ref [9] and [13] for review). When a structural material contains micro- and nano-scaled components, as is the case with hard biological materials, size-dependent mechanical properties of constituent materials may play a key role in the enhancement of the overall strength, stiffness, and fracture resistance and need to be incorporated into models to accurately predict structural response.

The design principles offered by hard biological materials can help guide the creation of mechanically robust and lightweight structural materials. In this work we apply and en-

hance this concept by first determining the dimensions at which a material would exhibit improved material properties and then creating a 3-dimensional architecture with constituents at these length scales. This approach requires at least three conditions to hold. First, the constituent material must exhibit better mechanical properties when reduced to nanoscale. Examples of such classes of materials include metallic glasses and ceramics, which have been shown to demonstrate a suppression of catastrophic failure and increase of strength at the nano-scale[9,14–17] and single crystalline metals, whose strengths increase according to a power law with size reduction[13]. Recent literature suggests that poly-/nano-crystalline metals may not offer beneficial properties because they have been shown to become weaker at the nanoscale[18,19]. Second, the construction of an architected structure with material constituents at these dimensions requires the existence of high-precision nano-fabrication techniques which are capable of producing such features in 3 dimensions. Finally, the reduction of component size must not degrade the structural response of the architected meta-material.

We report fabrication, characterization, and mechanical properties of periodically-arranged hollow titanium nitride (TiN) nanolattices with the dimensions of individual components spanning from nanometers to hundreds of microns, close to those of the cell walls in diatom organisms (Figure 1). It should be noted that our structure is constructed with hollow tubes as opposed to that many natural biominerals consists of either solid or porous materials[3]. The fabrication process consists of the following steps: (1) digital design of a 3-dimensional structure (Figure 1**d** and **e**), (2) direct laser writing (DLW) of this pattern into a photopolymer via two-photon lithography (TPL) to create free-standing 3-dimensional solid polymer skeletons, (3) conformal deposition of TiN via atomic layer deposition (ALD), and (4) etching out of the polymer core to create hollow ceramic nanolattices (Figure 1**f, g**: 3D Kagome unit cell, **h, i**: Octahedral unit cell). The octahedral nanolattice in Figure 1**d** and **e** was designed using a series of tessellated regular octahedra connected at their vertices. Each octahedron was made up of 7 μm-long hollow struts with elliptical cross sections and wall thicknesses of 75 nm (see inset in Figure 1**i**). The resulting structure was approximately 100 μm in each direction. The characteristic microstructural length scale of TiN, represented by its grain size, was between 10 and 20 nm, as can be seen in the dark-field transmission electron microscope (TEM) image in Figure 1**j**. Figure 1 also contains scale bars showing all relevant sizes within these structures.

We conducted in-situ compression experiments on the octahedral unit cell by applying an axial load along the vertical axes of the unit cells. The experimentally obtained force vs. displacement data was input into a finite element method (FEM) framework to estimate the local stresses within the structure under the applied load. Results revealed the attainment of von Mises stresses of 2.50 GPa, a value close to the theoretical strength of TiN[9,20,21], without failure. We discuss the emergence of such high strength and failure resistance in the context of weakest link theory in brittle materials, which may provide insight into the origins of enhanced damage tolerance of biological organisms.

The hollow ceramic nanolattices described here represent a departure from existing literature in several ways[22]. For example, in the previous work, hollow micro-latticces were fabricated using a UV-lithography mask-based technique, which limited structural dimensions to a minimum of 100 μm and generated periodic lattices with the maximum height on the centimeter order[22]. The two-photon lithography fabrication technique used in this work enables attaining feature resolution more than two orders of magnitude smaller than in the process described in Ref [22] and allows for generating any arbitrary geometry, not limited to periodicity. The subsequent deposition step in this work was accomplished via ALD, which offers high integrity of the film, a precise control of the microstructure, and the ability to deposit non-metals like TiN. This is in contrast to electro-less plating of nanocrystalline Ni in the micro-lattices[22] or other mechanical meta-materials made out of the solid polymers[23,24]. Another distinction of the rigid nano-lattices as compared with the micro-sized 3D structures is that the coating thickness in the latter would render them to be prohibitively weak when the wall thicknesses were reduced to the dimensions where a size-effect would be observed.

Figure 2 shows the results of in-situ monotonic (**a** – **d**) and cyclic (**e** – **h**) loading experiments on a single octahedral unit cell of the fabricated hollow nanolattice. Each unit cell was vertically compressed by applying a load to the apex using a flat punch indenter tip. The load–displacement curve for monotonic loading (Figure 2**a**) shows that the sample deformed elastically until the onset of non-linearity (indicated by the arrow) and subsequently failed at a maximum load of ∼150 μN (marked by **II**). The load–displacement plot in Figure 2**a** displays vertical displacement of the four upper struts less the elastic vertical deflection of the medial nodes measured from the recorded video (see Supplementary Movie S1). This net displacement of the upper beams was used as the boundary condition in the simplified four beam model in the finite element analysis. The SEM images in Figures 2**b** through

d depict the deformation morphology evolution during the experiment: (**b**) corresponds to point **I** in the load-displacement data shown in (**a**) and depicts the initial structure before any load was applied; (**c**) corresponds to **II**, the point of maximum applied load; and (**d**) corresponds to **III**, the point after failure. These images show that the deformation was accommodated mostly by bending and twisting of the diagonal truss members until the unit cell failed catastrophically at the nodes and along the mid-sections of the struts, noted by the arrows in Figure 2**d**.

Figure 2**e** shows the load–displacement data from the cyclical loading experiment performed on a different single octahedral unit cell. Three consecutive sets of loading cycles were performed, each consisting of 11 individual loading–unloading cycles up to a total displacement of 350 nm (beam deformation + base deflection), with a maximum load of 150 μN, followed by an unloading down to 10% of the maximum load attained in each previous cycle. The data in Figure 2**e** shows the net displacement of the upper beams corrected for the medial node deflection. SEM images of the deformed structures shown in Figures 2**f** – **h** were obtained after each set of cycles and revealed that the residual bending of the beams after complete unloading gradually increased with the number of cycles. The plot in Figure 2**e** shows a hysteresis between loading and unloading paths, as well as a residual displacement after each load-unload cycle, which implies that some permanent deformation, possibly nano-cracking, occurred. This is consistent with SEM images in Figures 2**f**–**h**, which have arrows pointing to the permanently deformed regions. The loading data in each cycle is characterized by elastic loading followed by a non-linear response, whose onset occurred at progressively lower applied forces: from 114 μN to 84 μN after 11 cycles and 41 μN after 22 cycles. The extent of the non-linear response increased from 125 nm after the 1st set of cycles to 160 nm after last. The load at the transition to non-linearity decreased with cycling, which may have been due to the formation and propagation of nano-cracks. The observed hyperelasticity in the loading and unloading cycles was likely a result of bifurcation caused by torsional buckling within the tubes[25,26]. FEM simulations revealed a similar bifurcation response at the onset of lateral deflection, which implies that hyperelasticity was a structural response and not a material response.

Figure 3 presents von Mises stress distribution and deformation morphology within a unit cell, calculated using finite element framework under the same maximum load of 0.15 mN as in the experiments. The simulated unit cell included the four beams that constitute the

upper half of the structure, with a rigid boundary condition applied to the bottom. This boundary condition is reasonable because the 8 beams that meet at the lower node create a very stiff elastic support that can be approximated to be rigid. We simulated two slightly different structures, one with all beams perfectly jointed at a common center (Figure 3**a**), and the other with a small counterclockwise offset at the node (Figure 3**b** insets). In the first case, the strut members deflected vertically with no lateral bending. This is not what was observed experimentally. Rather, the computed deformation morphology of the slightly offset structure, shown in Figure 3**b**, was found to accurately reproduce the twisting and bending of the beams in the experiments (Figure 2**c**), which is likely a result of an imperfect junction at the nodes. Qualitatively, when the beams do not meet at a common center, any small offset induces an additional moment in the center of the structure, which leads to a lateral bending moment and axial torsion in the beams. These additional moments and torsions facilitate the onset of buckling in the beams. The deflection profiles of the offset structures observed in experiments and in FEM simulations (Figure 3**b**) are consistent with this line of reasoning.

The Young's modulus of TiN, which was extracted from the simulations based on the experimentally observed deflection of the beams, was 98 GPa, a value on the lower end of the reported range[27]. The Young's moduli of ceramics have been shown to vary as a function of processing conditions and porosity[28,29]; it is likely that atomic layer deposition onto polymers produces films with lower density than those on hard substrates forming nano-sized flaws because gas-phase reactants diffuse into the substrate[30]. A recent experimental and computational study demonstrated that the strength of brittle nanocrystalline nanomaterials was unaffected by the presence of nano-sized surface notches[31]. This implies that the strength of the ALD–TiN in this work is likely insensitive to the possible imperfections within the film. When the maximum load of 0.15 mN is applied, the maximum von Mises stress in the beam (excluding the geometric concentrations at the central node) was calculated to be approximately 2.50 GPa, which corresponds to a maximum tensile stress of 1.75 GPa and a strain of 1.8%. This tensile strength of TiN is an order of magnitude higher than that of most brittle ceramics, whose typical values are on the order of a few tens to hundreds of MPa[21,27,32].

Titanium nitride is a typical ceramic whose mechanical behavior is characterized by brittle failure that occurs at the pre-existing flaws[33]. Failure in ceramics generally initiates at

an imperfection with the highest stress concentration, such as a crack or a void. Fracture strength of typical ceramics is a few orders of magnitude lower than those predicted theoretically for a perfect material[20]. The observed high tensile strength of 1.75 GPa and the bending strain of 1.8% that were attained by the TiN struts in this work are unusually high for a nanocrystalline ceramic. This high strength might be understood by considering the competing effects of microstructural and external local stress fields on strength and failure initiation[31].

In macroscopic brittle materials, the fracture strength, σ^f, is defined by the crack geometry and size,

$$\sigma^f = \frac{K_c}{\sqrt{\pi a}}, \tag{1}$$

where K_c is the fracture toughness and a is the initial flaw size[20]. Eq. 1 shows that the strength of materials is inversely proportional to the square-root of the size of pre-existing flaws, which serve as weak spots for failure initiation and reduce material strength. In large samples, the wide statistical distribution of flaw sizes leads to a relatively high probability of finding a weak spot, and the material will break at a relatively low applied stress. In smaller samples, the distribution of flaw sizes is narrower, which lowers the probability of finding a large flaw and shifts the strength of the weakest link up. In sufficiently small nanocrystalline samples, the low probability of finding a weak external flaw and the blunting of the notch tip by nucleated dislocations render the stress concentration at the external flaws comparable to those within the microstructure, i.e. grain boundary triple junctions[31]. In these small samples, usually with nanometer dimensions, failure has been shown to initiate at the weakest spot, i.e. a location with the highest stress concentration, internally or externally[31]. Fracture strength of materials whose failure is described by the weakest link theory is commonly explained by Weibull statistics[20]. The probability of finding the weakest spot inversely scales with the sample volume, V. Weibull analysis predicts the fracture strength to be proportional to $(1/V)^{1/m}$. Here, m is the Weibull modulus, a measure of statistical variability where higher m corresponds to a wider statistical distribution of strength[20]. The volume of hollow TiN nanolattices with can be approximated to be $V \sim A \times t$, where A is the total surface area and t is the wall thickness. When the wall thickness of hollow TiN tubes is the only varying geometric dimension, the fracture strength of TiN walls becomes

$$\sigma^f \propto \left(\frac{1}{t}\right)^{1/m}. \tag{2}$$

Eq 2 implies that nanolattices with thinner walls are expected to be stronger up to a critical length scale, t^*, because the attainable stress in any material is bounded by a theoretical upper limit, often called the ideal fracture strength. A reasonable approximation of this strength may be between $E/2\pi$ and $E/30$;[9,20,21] which represents the atomic bond strength of a material along the tensile loading direction, and is independent of sample size[20]. Figure 4 depicts an illustrative plot of strength as a function of sample thickness, which shows the intersection of the theoretical strength and that described by Eq 2 at the critical thickness of t^*. This plot illustrates the saturation of the fracture strength at the theoretical upper limit in samples with dimensions lower than t^*. Our FEM simulations on samples with the same material properties and of the same geometry as in the experiments predict the maximum tensile stresses in the TiN struts to be 1.75 GPa, close to the theoretical elastic limit of 3.27 GPa (estimated by $E/30$ with E=98 GPa), which suggests that the wall thickness of 75 nm in the hollow TiN nanolattices might be close to the critical length scale. This line of reasoning serves as a phenomenological first order type of model, which may help explain the attainment of unusually high tensile strengths in the thin TiN walls without failure. Rigorous theoretical studies on uncovering the deformation mechanisms in nano-sized solids, which may or may not contain internal stress landscapes, are necessary to capture the complex physical phenomena associated with their deformation and failure.

This work presents the development of a multi-step nano-fabrication process to create 3-dimensional hollow rigid lattices, or structural meta-materials, whose relative density is on the order of 0.013 (similar to aerogels) and whose characteristic material length scales span from 10 nm to 100 μm. In-situ compression experiments on individual unit cells in combination with FEM simulations revealed that these meta-materials did not fracture under the applied load even after multiple loading cycles and attained tensile stresses of 1.75 GPa, which represents close to half of the theoretical strength of TiN. We attribute the attainment of such exceptionally high strength in TiN to the low probability of pre-existing flaws in nano-sized solids. Failure in such materials initiates at a weakest link, which is determined by the competing effects of stress concentrators at surface imperfections and local stresses within the microstructural landscape. These findings may offer the potential of applying hierarchical design principles offered by hard biological organisms to creating damage-tolerant lightweight engineering materials.

METHODS

A. Fabrication

Hollow TiN nanolattices were fabricated using a multi-step negative pattern process, which involved TPL (two-photon lithography), DLW (direct laser writing), ALD (atomic layer deposition), and O_2 plasma etching. The initial polymer scaffold was fabricated through a TPL DLW process in IP-Dip 780 photoresist with a speed of 50 μm/sec and laser power of 10 mW using the Photonic Professional DLW system (Nanoscribe GmbH, Germany). These structures were then conformally coated one monolayer at a time with TiN using an Oxford OpAL ALD system (Oxfordshire, UK) at 140°C. The deposition was performed by sequentially cycling through the following steps: i) flowing the reactant dose of Titanium Tetrachloride ($TiCl_4$) precursor for 30 ms, ii) purging the system for 5 sec, iii) plasma treatment with an N_2/H_2 gas mixture (25 sccm/25 sccm) for 10 sec, and iv) purging the system for an additional 5 sec. This process was repeated until a 75 nm thick layer was deposited. The TiN coating was then removed along an outer edge of the structure using focused ion beam (FIB) in the FEI Nova 200 Nanolab to expose the polymer core, which was subsequently etched out in a barrel oxygen plasma etcher for 3 hours under 100 W and 300 sccm oxygen flow.

B. Mechanical Characterization

Individual unit cells were quasi-statically compressed by applying a load to the top node along the vertical axis using InSEM^{TM}(Nanomechanics, Inc., Tennessee), an in situ nanomechanical instrument previously referred to as SEMentor (See Ref [16] for the specification of the instrument). Samples were deformed at a nominal displacement rate of 10 nm/sec until failure during monotonic experiments; cyclic experiments consisted of 11 loadings to total displacements (beam deformation + medial node deflection) of 350 nm followed by unloading to 10% of the maximum load in the previous cycle. Prior to the tests, the instrument was stabilized for at least 12 hours to minimize thermal drift. Typical thermal drift rate of this instrument is below 0.05 nm/sec, which would contribute less than 0.5% to the total displacement.

C. Finite Element Analysis

Sample geometry used in FEM simulations was generated using CAD software Solid-Works, with dimensions measured from SEM images of the actual structure. The members that make up the truss structure in the model were hollow elliptical tubes with a height of 1.2 μm, a width of 265 nm, and a wall thickness of 75 nm. The tubes were made to converge at the central nodes of the structure with a uniform counterclockwise offset of 20 nm, as in the fabricated structures (see inset in Figure 3**b**). Unit cell was simplified to only include the upper four bars of the structure to reduce the computational cost. A tetrahedral mesh was generated using the finite element software ABAQUS, and a nonlinear geometry solver was implemented to capture large deflections of the structure. Upon loading, the mesh was manually refined until the stresses converged, with a final average mesh density of roughly 400,000 elements/μm^3 and a higher concentration of elements toward the central node. All four upper beams of the structure were modeled to ensure that the observed response was due to the truss member interactions and not to the imposed boundary conditions.

AUTHOR CONTRIBUTIONS

D.J. and L.M. fabricated the samples and conducted all experiments. F.G. deposited TiN in ALD at the Jet Propulsion Laboratory. L.M. performed finite element analysis. J.R.G. conceived of the research and provided guidance. All authors analyzed the data, discussed the results and wrote the manuscript.

[1] Kröger, N. Prescribing diatom morphology: toward genetic engineering of biological nanomaterials. *Current opinion in chemical biology* **11**, 662–9 (2007).

[2] Aizenberg, J. *et al.* Skeleton of Euplectella sp.: structural hierarchy from the nanoscale to the macroscale. *Science* **309**, 275–8 (2005).

[3] Weaver, J. C. *et al.* Hierarchical assembly of the siliceous skeletal lattice of the hexactinellid sponge Euplectella aspergillum. *Journal of structural biology* **158**, 93–106 (2007).

[4] Hamm, C. E. *et al.* Architecture and material properties of diatom shells provide effective mechanical protection. *Nature* **421**, 841–3 (2003).

[5] Yang, W. *et al.* Natural flexible dermal armor. *Advanced materials* **25**, 31–48 (2013).

[6] Weiner, S. & Wagner, H. D. THE MATERIAL BONE: Structure-Mechanical Function Relations. *Annual Review of Materials Science* **28**, 271–298 (1998).

[7] Kamat, S., Su, X., Ballarini, R. & Heuer, A. Structural basis for the fracture toughness of the shell of the conch Strombus gigas. *Nature* **405**, 1036–40 (2000).

[8] Jäger, I. & Fratzl, P. Mineralized collagen fibrils: a mechanical model with a staggered arrangement of mineral particles. *Biophysical journal* **79**, 1737–46 (2000).

[9] Gao, H., Ji, B., Jager, I. L., Arzt, E. & Fratzl, P. Materials become insensitive to flaws at nanoscale: lessons from nature. *Proceedings of the National Academy of Sciences of the United States of America* **100**, 5597–600 (2003).

[10] Bach, K. *Radiolaria, IL 33* (Institute for Lightweight Structures, Stuttgart University, 1990).

[11] Sarikaya, M. & Aksay, I. A. Nacre of abalone shell: a natural multifunctional nanolaminated ceramic-polymer composite material. *Results and problems in cell differentiation* **19**, 1–26 (1992).

[12] Gibson, L. J. & Ashby, M. F. *Cellular solids: Structure and properties.* 2 (Cambridge University Press, Cambridge, 1999), 2nd edn.

[13] Greer, J. R. & De Hosson, J. T. Plasticity in small-sized metallic systems: Intrinsic versus extrinsic size effect. *Progress in Materials Science* **56**, 654–724 (2011).

[14] Jang, D. & Greer, J. R. Transition from a strong-yet-brittle to a stronger-and-ductile state by size reduction of metallic glasses. *Nature Materials* **9**, 215–219 (2010).

15 Korte, S., Barnard, J., Stearn, R. & Clegg, W. Deformation of silicon Insights from microcompression testing at 25500C. *International Journal of Plasticity* **27**, 1853–1866 (2011).

16 Östlund, F. *et al.* Brittle-to-Ductile Transition in Uniaxial Compression of Silicon Pillars at Room Temperature. *Advanced Functional Materials* **19**, 2439–2444 (2009).

17 Matoy, K. *et al.* A comparative micro-cantilever study of the mechanical behavior of silicon based passivation films. *Thin Solid Films* **518**, 247–256 (2009).

18 Jang, D. & Greer, J. R. Size-induced weakening and grain boundary-assisted deformation in 60 nm grained Ni nanopillars. *Scripta Materialia* **64**, 77–80 (2011).

19 Gu, X. W. *et al.* Size Dependent Deformation of Nanocrystalline Pt Nanopillars. *Nano letters* (2012).

20 Meyers, M. A. & Chawla, K. K. *Mechanical behavior of materials* (Prentice-Hall, Inc., New Jersey, 1998), 1st edn.

21 Kingery, W. D., Bowen, H. K. & Uhlmann, D. R. *Introduction to Ceramics* (John Wiley & Sons, Inc., New York, 1975), 2nd edn.

22 Schaedler, T. A. *et al.* Ultralight Metallic Microlattices. *Science* **334**, 962–965 (2011).

23 Bückmann, T. *et al.* Tailored 3D mechanical metamaterials made by dip-in direct-laser-writing optical lithography. *Advanced materials* **24**, 2710–4 (2012).

24 Kadic, M., Buckmann, T., Stenger, N., Thiel, M. & Wegener, M. On the practicability of pentamode mechanical metamaterials. *Applied Physics Letters* **100**, 191901 (2012).

25 Law, K. & Gardner, L. Lateral instability of elliptical hollow section beams. *Engineering Structures* **37**, 152–166 (2012).

26 Li, C., Ru, C. Q. & Mioduchowski, A. Torsion of the central pair microtubules in eukaryotic flagella due to bending-driven lateral buckling. *Biochemical and biophysical research communications* **351**, 159–64 (2006).

27 Shackelford, J. F. & Alexander, W. *Materials Science and Engineering Handbook* (CRC Press, Inc., Boca Raton, 2000), 3rd edn.

28 Andrievski, R. Physical-mechanical properties of nanostructured titanium nitride. *Nanostructured Materials* **9**, 607–610 (1997).

29 Lim, J.-W., Park, H.-S., Park, T.-H., Lee, J.-J. & Joo, J. Mechanical properties of titanium nitride coatings deposited by inductively coupled plasma assisted direct current magnetron sputtering. *Journal of Vacuum Science & Technology A: Vacuum, Surfaces, and Films* **18**, 524

(2000).

30 George, S. M. Atomic layer deposition: an overview. *Chemical reviews* **110**, 111–31 (2010).

31 Gu, X. W., Wu, Z., Zhang, Y.-W., Srolovitz, D. J. & Greer, J. R. Flaw-Driven Failure in Nanostructures. Submitted (2013).

32 Wiederhorn, S. M. Brittle Fracture and Toughening Mechanisms in Ceramics. *Annual Review of Materials Science* **14**, 373–403 (1984).

33 Kumar, S., Wolfe, D. & Haque, M. Dislocation shielding and flaw tolerance in titanium nitride. *International Journal of Plasticity* **27**, 739–747 (2011).

FIGURES
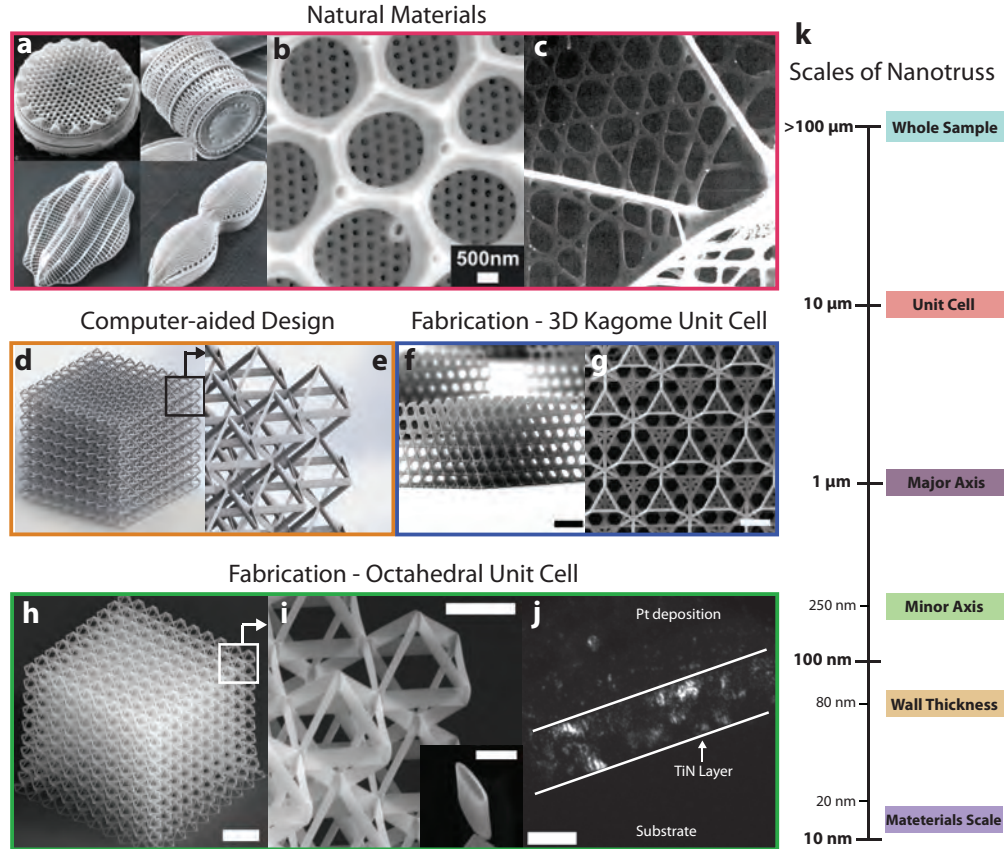
Figure 1. **Skeletal natural biological materials vs. TiN nanolattices. a, b,** SEM images of silicified cell walls with periodic lattice structures from different diatom species (Images are reprinted from Ref [1] with permission) and **c,** optical image of radiolaria with Kagome lattice (reprinted from Ref [10] with permission). **d, e,** Computer-aided design of octahedral nanolattices. **f − h,** SEM image of fabricated nanolattice with 3-dimensional Kagome unit cell. **h − j,** SEM (**h, i**) and TEM dark-field (**j**) images of engineering hollow nanolattice synthesized with TiN. Inset in **i** shows the cross-section of a strut. TiN thin film in **j** was deposited in the same batch with nanolattice samples. **k,** Schematic representation of the relevant dimensions of such fabricated nanolattices. Scale bars, b: 500 nm, h: 20 μm, fi 5 μm (inset: 1 μm), j: 20 nm
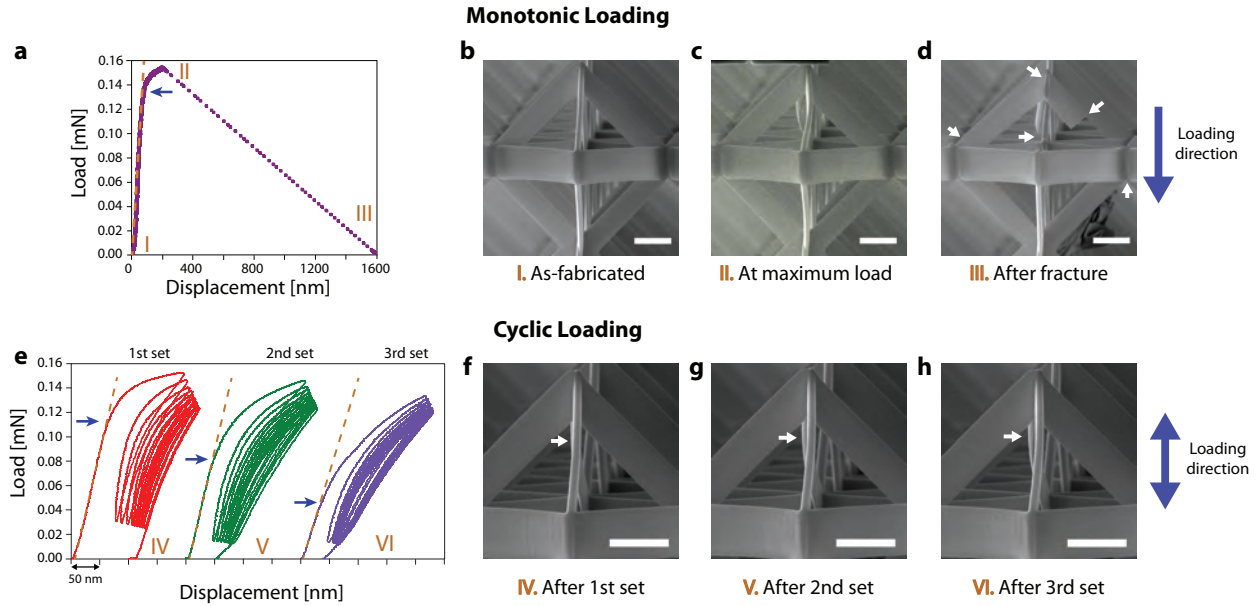
Monotonic Loading

Cyclic Loading

Figure 2. **Compression experiments on a single unit cell. a, e,** Load vs. displacement data from monotonic and cyclic loading experiments. Arrows in **e** indicate onset of non-linearity. **b –
d,** SEM images taken at (**b**) zero and (**c**) maximum loads and (**d**) after failure during a monotonic loading experiment. Arrows in **d** point to the location of fracture. **f – h,** SEM images taken after each cycle during a cyclic loading experiment. Arrows in **f**–**h** shows permanent deformation of the beam after each loading cycle. All scale bars: 1 μm

18

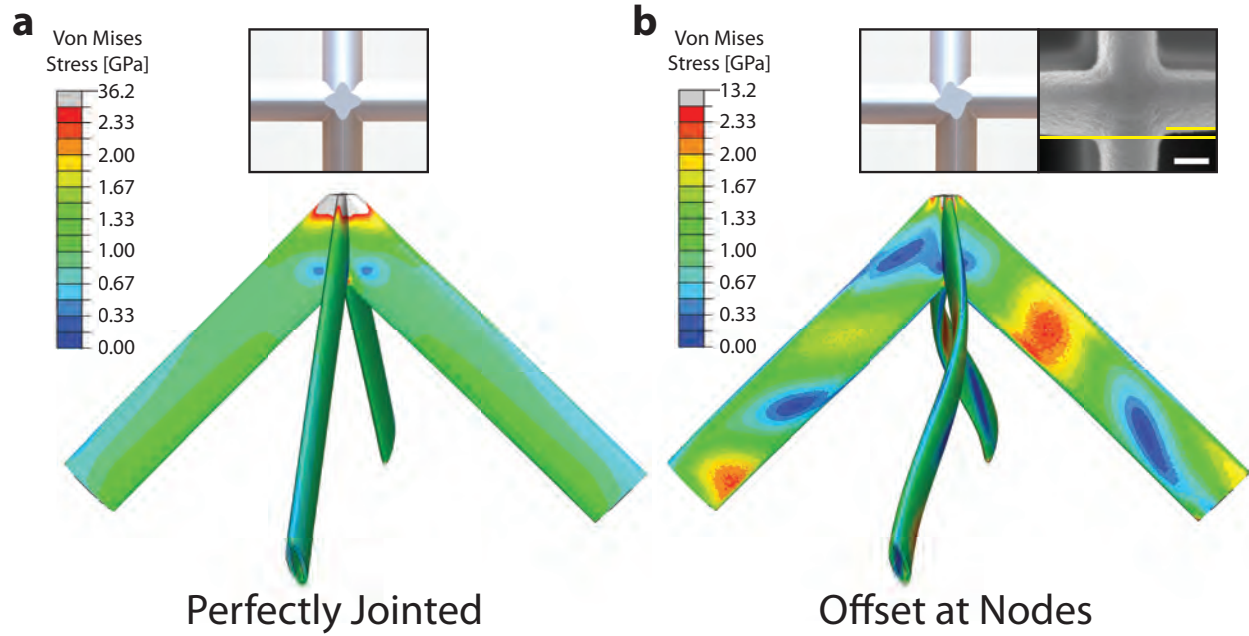**Figure 3. Finite element analysis of the top half of unit cell. a, b** Deformation morphology and von Mises stress distribution within individual struts, **a**, with the beams perfectly jointed at a common center and, **b**, with nodal offsets. The insets in **a** and **b** (left) show the top-down images of the nodes in the FEM model and the right inset in **b** shows the corresponding SEM image from the real nanolattice. The scale bar in the inset in **b** is 200 nm long.
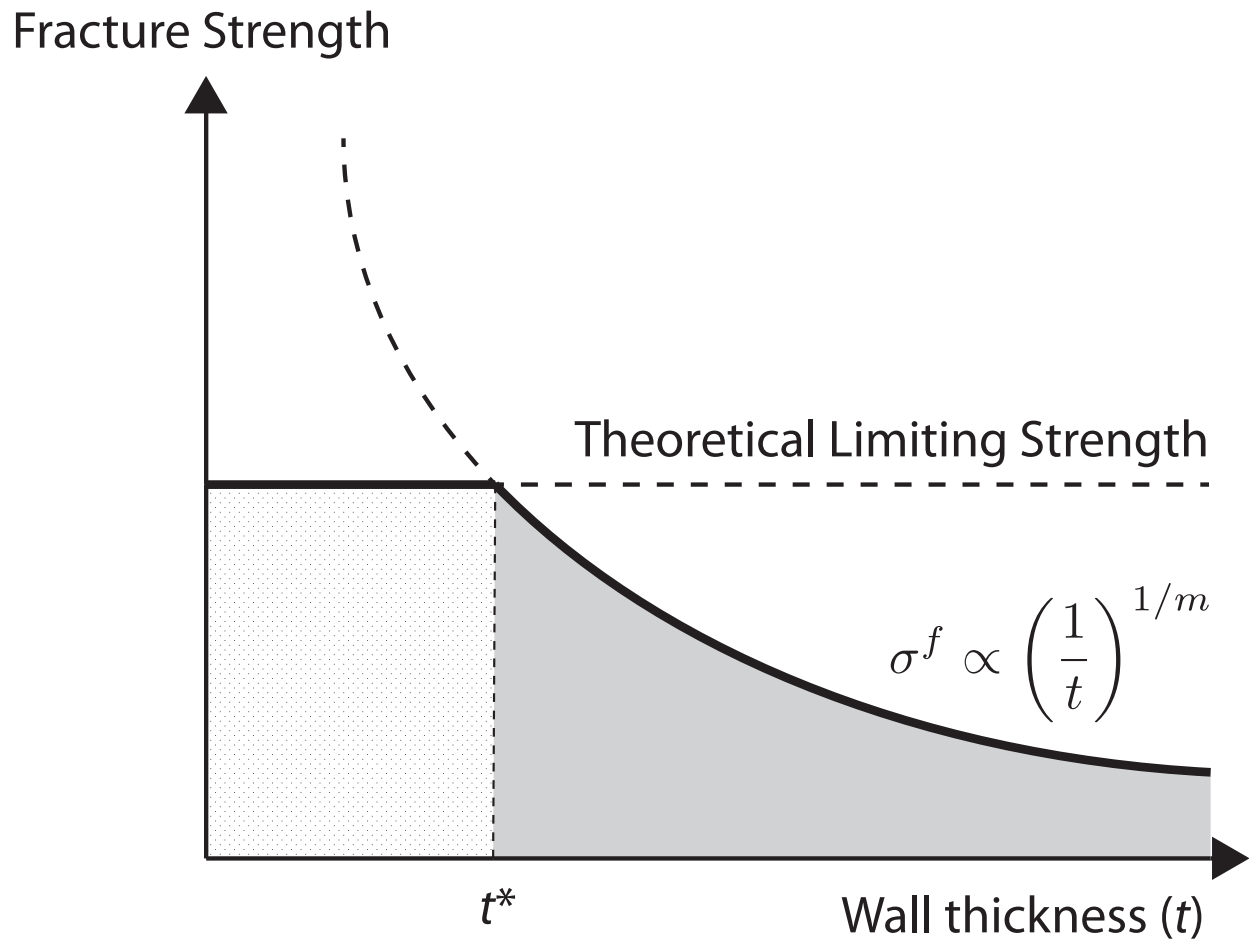
Figure 4. **Schematic representation of theoretical strength, which is independent of sample size, and fracture strength described by Weibull statistics.**